

Article

Synthesis, Spectral Characterization, and Structural Modelling of Di- and Trinuclear Iron(III) Monensinates with Different Bridging Patterns

Nikolay Petkov ^{1,*}, Alia Tadjer ¹, Svetlana Simova ², Zara Cherkezova-Zheleva ³, Daniela Paneva ³,
Radostina Stoyanova ⁴, Rositsa Kukeva ⁴, Petar Dorkov ⁵ and Ivayla Pantcheva ^{1,*}

¹ Faculty of Chemistry and Pharmacy, Sofia University St. Kliment Ohridski, 1164 Sofia, Bulgaria; tadjer@chem.uni-sofia.bg

² Institute of Organic Chemistry with Centre of Phytochemistry, Bulgarian Academy of Sciences, 1113 Sofia, Bulgaria; svetlana.simova@orgchm.bas.bg

³ Institute of Catalysis, Bulgarian Academy of Sciences, 1113 Sofia, Bulgaria; zzhel@ic.bas.bg (Z.C.-Z.); daniela@ic.bas.bg (D.P.)

⁴ Institute of General and Inorganic Chemistry, Bulgarian Academy of Sciences, 1113 Sofia, Bulgaria; radstoy@svr.igic.bas.bg (R.S.); rositsakukeva@yahoo.com (R.K.)

⁵ Research and Development Department, Biovet Ltd., 4550 Peshtera, Bulgaria; p_dorkov@biovet.com

* Correspondence: ahnp@chem.uni-sofia.bg (N.P.); ahip@chem.uni-sofia.bg (I.P.); Tel.: +359-2-8161446 (N.P. & I.P.)

Abstract: In the present study, we report the solid-state isolation and structural characterization of novel iron(III) complexes of the veterinary antibiotic monensin. Monensic acid ($\text{MonH} \times \text{H}_2\text{O}$) forms a dinuclear complex of composition with $\text{FeCl}_3 [\text{FeCl}(\text{Mon})_2]_2$ (**1**), while its interaction with FeSO_4 leads to the isolation of a triangular oxo-ferric coordination species $[\text{Fe}_3\text{O}(\text{Mon} \times \text{H}_2\text{O})_6(\text{H}_2\text{O})_2(\text{OH})]$ (**2**). During the procedure resulting in **2**, oxidation of the Fe(II) ions by atmospheric oxygen was observed. In the presence of organic bases, both complexation reactions proceeded to successfully deprotonate the carboxylic function of the ligand. Iron(III) complexes **1** and **2** were characterized by IR, EPR, NMR, and Mössbauer spectroscopies as well as with thermal (TG-DTA/MS) and elemental analyses. In addition, the structures of the two coordination compounds were modelled and selected calculated parameters were compared with the experimental results. The biological assay revealed the enhanced antibacterial potential of the newly obtained complexes against the Gram-positive aerobic microorganisms *Bacillus cereus* and *Bacillus subtilis*.

Keywords: polyether ionophore; antibacterial iron(III) complexes; antiferromagnetism; DFT modelling



Citation: Petkov, N.; Tadjer, A.; Simova, S.; Cherkezova-Zheleva, Z.; Paneva, D.; Stoyanova, R.; Kukeva, R.; Dorkov, P.; Pantcheva, I. Synthesis, Spectral Characterization, and Structural Modelling of Di- and Trinuclear Iron(III) Monensinates with Different Bridging Patterns. *Inorganics* **2024**, *12*, 114. <https://doi.org/10.3390/inorganics12040114>

Academic Editors: Sunčica Roca and Monika Kovačević

Received: 18 March 2024

Revised: 8 April 2024

Accepted: 11 April 2024

Published: 15 April 2024



Copyright: © 2024 by the authors. Licensee MDPI, Basel, Switzerland. This article is an open access article distributed under the terms and conditions of the Creative Commons Attribution (CC BY) license (<https://creativecommons.org/licenses/by/4.0/>).

1. Introduction

Iron ions play a significant role in almost all living organisms [1]. They are vital for transporting oxygen, activating various substrates, and assisting in electron transfer reactions. Most of these processes occur due to the versatile coordination ability of both Fe(II) and Fe(III). The chemistry and biochemistry of ferric complexes are well known and have been subject to intensive reviewing over the years [2–5]. Iron(III) can form a wide variety of structural arrangements ranging from mono- to polynuclear coordination species with ligands involving diverse donor atoms and exhibiting different denticity. The literature overview reveals that a number of iron(III) complexes contain carboxylate ligands and exist as di- or trinuclear coordination species. In the first category, the carboxylate group participates as a terminal ligand in the formation of diamond-core $\text{Fe}_2(\mu_2\text{-O})_2$ complexes with hydroxide/alkoxide bridges or acts as a $(\mu\text{-}\eta_1\text{:}\eta_1)$ -link in both symmetric and asymmetric di-iron species [6–16]. Although rare, acetate complexes of various metal ions containing μ_2 -aqua or μ_2 -alcohol linkers are also known [17–25]. The trinuclear iron(III) carboxylates can be found mainly as oxo-ferric complexes adopting the typical triangular acetate structure [26–29]. In the above-mentioned constructs, three types of carboxylate

coordination modes with respect to the isolated iron centre can be realised (Figure 1), excluding the pure metal–ligand ionic bond: monodentate, bidentate, and bridging [30,31]. Which configuration will prevail in the corresponding coordination species depends on many factors such as the overall ligand structure (i.e., the presence of other functional groups), the reaction conditions, the solvent effect, the metal salt counterion, etc.

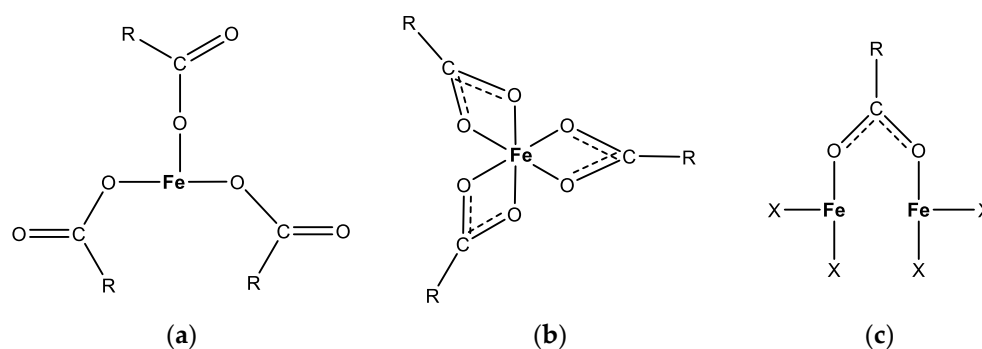


Figure 1. The possible (a) monodentate, (b) bidentate, and (c) bridging coordination patterns of the carboxylate group to iron(III) cation(s).

In addition to the rich and diverse coordination chemistry of iron that makes it suitable for a large variety of functions within biological systems [32], its metabolism was found to be crucial also for the life cycle of cancer cells, triggering ferroptosis—a recently described form of regulated cell death caused by iron-dependent lipid peroxidation [33]. The ferroptosis is driven by various mechanisms, including the following:

- (i) glutathione level reduction and decreased activity of glutathione peroxidase, which results in the deposition of harmful lipid-reactive oxygen species (L-ROS) from polyunsaturated fatty acids in the presence of high concentrations of iron ions, thus promoting cell death [34];
- (ii) overexpression of transferrin receptor 1 (TFR1) and decrease in ferritin levels, since the upregulation of TFR1 is detected in many malformations such as glioblastoma, leukaemia, breast cancer, ovarian cancer, hepatic cancer, thyroid cancer, and colorectal cancer [35];
- (iii) Fenton reaction that strongly depends on the intracellular iron concentration and can be a possible mechanism of ROS generation.

Ferroptosis has been suggested to be an endogenous anticancer mechanism providing new opportunities in the treatment of drug-resistant tumours. In this sense, any natural compound that can induce such regulated cell death can be treated as a potential anticancer agent [36,37]. Recently, it was shown that some members of the natural carboxylic polyether ionophores—salinomycin and ironomycin—accumulate in lysosomes, sequester the lysosomal iron, and produce ROS in this organelle via Fenton reaction [38–40].

To gain deeper insight into the possible chemical interactions between polyether ionophores and Fe(II)/Fe(III), we initiated targeted research on the coordination ability of monensin and salinomycin (HL) to bind iron. Monensic acid (MonH, Figure S1) was selected as the most widely applied antibiotic in veterinary medicine, and salinomycinic acid (SalH) was deemed as a promising anticancer agent. Our first findings led to the isolation and characterization of iron(III) monensinate and salinomycinic acid of composition $[\text{Fe}_3(\mu_3\text{-O})\text{L}_3(\text{OH})_4]$ [41]. Then, under completely different reaction conditions, two new Fe(III) coordination compounds of monensin were obtained with the involvement of the antibiotic carboxylate function in the complex formation. The reported iron(III) complexes of monensin can be described as dinuclear chloro-containing (1) and trinuclear oxo-ferric (2) coordination species. The experimental data reveal that the antibiotic ligand serves in a pure monodentate/bidentate or in a bridged bidentate coordination mode, with the involvement of a terminal alcohol group in the bidentate ones. Employing the experimental

and theoretical chemistry tools, we were able to derive reliable structures of these new iron(III) monensinates, combining various spectroscopies and the computational DFT method.

2. Results and Discussion

2.1. General Remarks

In the presence of organic bases (Et_4NOH or Et_3N), monensic acid effectively deprotonates and acts as a carboxylate monoanion in complexation reactions with metal ions of different oxidation states [41–45]. Monensinate reaction with FeCl_3 or FeSO_4 leads to the formation of new complexes which exhibit spectral properties characteristic of di- (1) and trinuclear (2) coordination species of iron(III), respectively. In addition, the formation of 1 is accompanied by co-precipitation of the mono-complex 1a (Figure S2). The complete set of experimental data is significantly different from that previously reported for iron(III) monensinate and salinomycinates [41], a fact indicating that we have prepared new ferric coordination compounds of the polyether ionophore monensin. The isolated solids 1 and 2 are amorphous without any sign of crystallinity, making their precise characterization difficult. The research methodology for structure elucidation described below is based on a series of spectroscopic techniques along with an appropriate computational chemistry protocol.

2.2. Physicochemical Properties of Complexes 1 and 2

2.2.1. Vibrational and Thermal Analysis

The IR spectra of 1 and 2 (Figure 2) reveal the deprotonation of monensin during its reaction with iron ions. The band of $\text{MonH} \times \text{H}_2\text{O}$ at 1710 cm^{-1} assigned to the carboxylic group is replaced by two new bands at 1592 and 1419 cm^{-1} in the spectrum of 1, attributed to the corresponding asymmetric and symmetric stretching vibrations of the carboxylate function. The multicomponent band at 1592 cm^{-1} was fitted with three Lorentzians (inset in Figure 1) thus assuming different coordination modes of the carboxylate moiety in the solid sample of complex 1 [46]. The areas of the sub-bands (1) at 1594 cm^{-1} (FWHM = 66 cm^{-1}) and (2) at 1554 cm^{-1} (FWHM = 46 cm^{-1}) are almost equal (ca. 45% for each component), whereas the area of sub-band (3) is noticeably smaller. It is supposed that 1 comprises two main types of carboxylates whose ligation varies to some extent due to the different values of $\Delta = \nu_{\text{asym}} - \nu_{\text{sym}}$, 175, and 135 cm^{-1} , respectively. The weak band at 1643 cm^{-1} (FWHM = 75 cm^{-1} , $\Delta = 224 \text{ cm}^{-1}$) is attributed to the presence of monensinate bound in another type of complex species. The latter probably exists as an impurity in the solid sample rather than as a constituent of the intrinsic structure of 1. As will be described further, this assumption is supported by the magnetic studies used for structural characterization of 1.

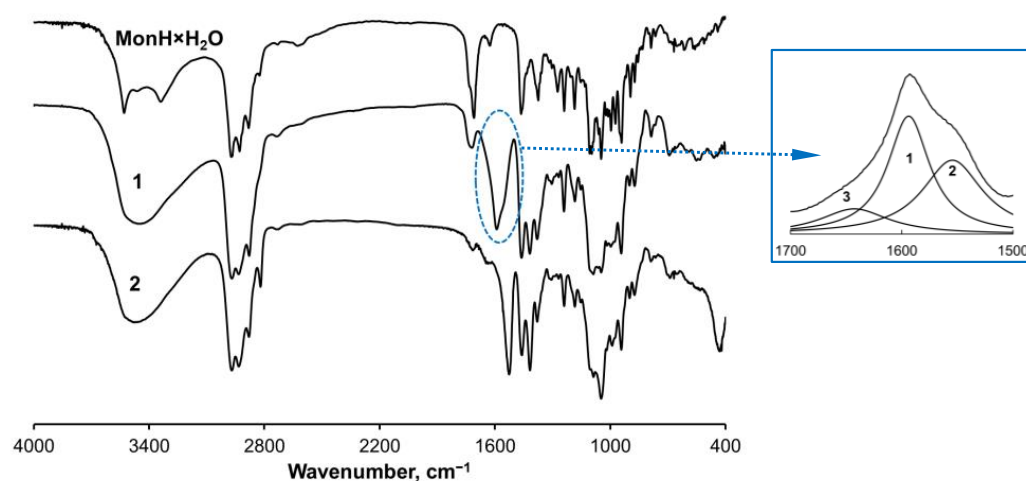


Figure 2. IR spectra of $\text{MonH} \times \text{H}_2\text{O}$ and complexes 1–2 in KBr pellets.

The spectrum of **2** also consists of two bands at 1527 and 1417 cm^{-1} , but the significantly smaller value of $\Delta = 110 \text{ cm}^{-1}$ points to a bridging coordination mode of the carboxylate moiety. Complex **2** exhibits intense characteristic bands below 1000 cm^{-1} which are absent in **1**. These vibrations are assigned to the formation of Fe-OH ($\delta_{\text{FeOH}} = 1047 \text{ cm}^{-1}$) and Fe-O ($\nu_{\text{FeO}} = 430 \text{ cm}^{-1}$) bonds, respectively. The bands in the range 4000–3000 cm^{-1} , related to asymmetric and symmetric stretching vibrations of OH-bonds in the water molecule (3530–3460 cm^{-1}), and ν_{OH} (3336 cm^{-1}) in $\text{MonH} \times \text{H}_2\text{O}$, broaden in the spectra of **1** and **2** (3450–3470 cm^{-1}) due to the OH-group's engagement in various intramolecular interactions.

No intense endothermic peaks below 185 °C were observed in the TG-DTA/TG-MS curves of complex **1** (Figure S3a), ruling out the presence of coordinated water molecule(s). In contrast, the endothermic peak at 104 °C in **2** refers to a two-step water loss, which is an indication of different types of water molecules present in the studied sample (Figure S3b).

Based on the IR and thermal data, combined with microanalysis results, it can be concluded that (i) monensin is bound as a monoanion in the structures of **1** and **2**; (ii) the molar metal-to-antibiotic ratio is 1:2 in both complexes; (iii) species **1** contains additional chloride ions, whereas a hydroxide anion and water ligands participate in the composition of **2**.

2.2.2. Magnetic Studies

The EPR spectra of complexes **1–2** are registered in the temperature range from 77 K (100 K) to 295 K (Figure 3). A general characteristic of the spectra at r. t. is the broad signal with $g = 2.02$, attributable to iron(III) ions, confirming the oxidation of Fe(II) under atmospheric conditions during the preparation procedure of **2**.

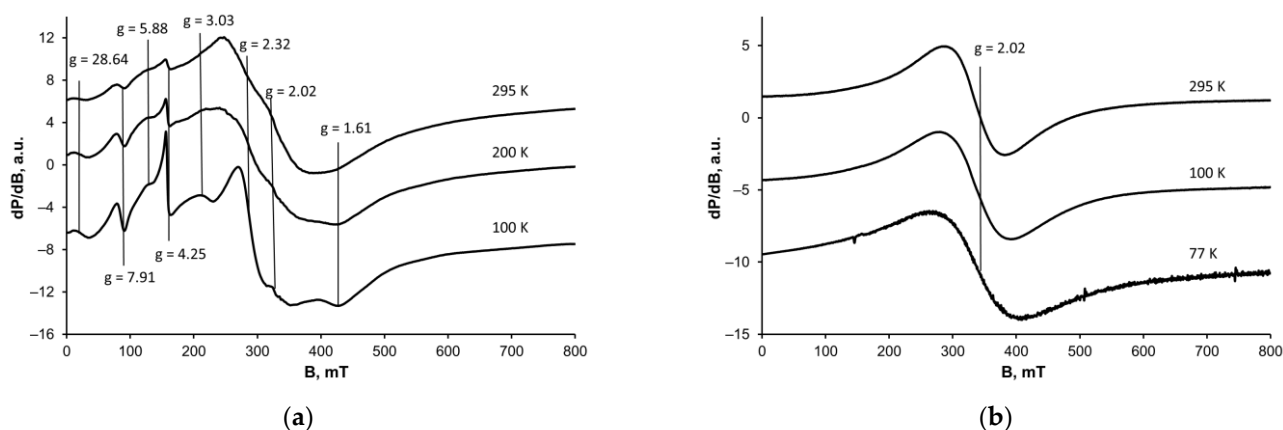


Figure 3. X-band solid-state EPR spectra of **1** (a) and **2** (b) registered in the range 77–293 K.

The peak-to-peak linewidth and intensity of the central signal ($g = 2.02$) in **1–2** show a well-defined tendency towards signal broadening with temperature decrease. Such a temperature dependence of the linewidth relates to an antiferromagnetic spin interaction of the metal centres, which becomes stronger at low temperatures.

The relatively broad signal with $g = 2.02$ observed for **1** is attributed to magnetically coupled Fe(III) ions [47]. It is accompanied by several extra signals which can be seen even at room temperature with effective g -factor values ranging from 28.64 to 1.61, labelled on Figure 3a. As the temperature decreases, the spectrum of **1** undergoes a transformation in which the less pronounced set of signals turns narrower at 100 K and becomes the main feature of the low temperature spectrum. On the other hand, the temperature behaviour of the signal with $g = 2.02$ is reversed. The result is that at 100 K its intensity is negligible compared with the intensities of the narrower lines set. Such a central field signal broadening can be attributed to the presence of closely spaced iron ions bound by a suitable ligand. Based on the composition data, we assume that chloride anions or hydroxyl groups

of the monensinate may play the role of such a linker between two metal centres to witness the observed EPR behaviour of **1**.

The set of lines that dominates the low-temperature spectrum of sample **1** refers to the fine structure of Fe^{3+} ions and its origin can be explained by allowed transitions with $\Delta m_s = 1$, although the existence of forbidden transition lines cannot be excluded either. These signals are ascribed to isolated $\text{Fe}(\text{III})$ ions placed in an axial symmetry field [48] and their presence can be attributed to the formation of the mono-complex **1a**, whose composition and structure will be discussed later. We could not eliminate **1a** despite our numerous attempts to purify the dinuclear complex. The presence of the assumed mono-species **1a** does not affect the overall elemental composition of **1**. The results are consistent with the IR-data, where the third weak band attributable to the asymmetric stretching of COO^- is assigned to the formation of a second type of coordination species present in a minor quantity.

For sample **2** the signal at $g = 2.02$ is the main spectral characteristic over the entire temperature range. The g -factor value remains constant in the whole temperature span (Figure 3b). The negative Curie–Weiss constant (-608 ± 12 K) and the signal broadening at low temperatures (95 mT at 295 K and 142 mT at 77 K) indicate the occurrence of exchange-coupled iron(III) ions.

To obtain additional information on the binding mode of monensin in **1–2**, we also performed NMR analysis, which might be strongly affected by the presence of paramagnetic ions, but in some cases can contribute to a deeper understanding of the properties of the metal complexes. We were unable to adjust the NMR settings and record any spectra of complex **2** using conventional NMR techniques, which may serve as indirect evidence that the studied monensinate sample contains paramagnetic iron(III) cations.

To our surprise, we recorded r. t. NMR spectra of **1** in CDCl_3 to observe a negligible shift of the ^{13}C signals compared with those of the uncoordinated monensinic acid (Table S1) at low sample concentration, while augmenting the concentration resulted in a significant signal broadening. We hypothesized that a possible dissociation of the dinuclear iron(III) complex may occur, inflicting structure breakdown under the solvent action [49]. To confirm this, we also measured the EPR spectrum of the same solution at 120 K (Figure 4). Experimental results reveal that there are relatively narrow signals (*ca.* 15–20 mT) with $g = 4.33$ and 2.01, which can be attributed to isolated Fe^{3+} ions placed in a low and in an octahedral symmetry, respectively [50]. The hump detected at 240 mT (as part of a broad signal with $g = 2.02$) is attributed to the presence of exchange-coupled $\text{Fe}(\text{III})$ ions. EPR data recorded both in solution and in the solid state confirm that **1** comprises different types of coordination species. At the current stage of research, we cannot explain the negligible effect of $\text{Fe}(\text{III})$ on monensin NMR signals, but it may be related to the lability/inertness of the coordination species formed—a phenomenon that deserves further investigation, which is beyond the scope of the present study.

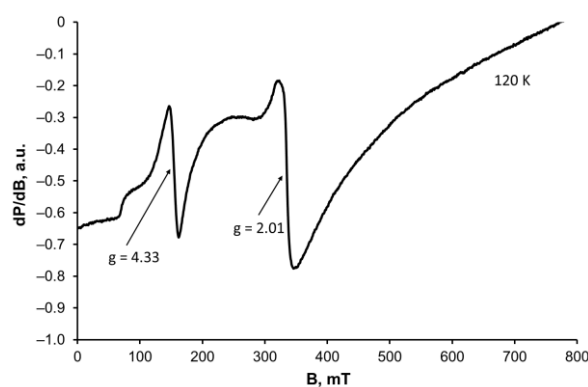


Figure 4. X-band EPR spectrum of frozen solution of **1** in CDCl_3 .

2.2.3. Mössbauer Studies

Monensin, as a representative of natural polyether ionophorous antibiotics, contains only O-donor atoms, so we suppose that the iron ions involved in the composition of complexes **1** and **2** will retain the high-spin configuration. Our hypothesis is confirmed by the subsequent Mössbauer studies performed at both room and liquid nitrogen temperatures.

The Mössbauer spectrum of **1** at 293 K consists of two asymmetric quadrupole signals that can be assigned to a minimum of two different types of iron ions. Consistent with the EPR data suggesting the presence of di- and mono-species, we decomposed the observed signals into three components by the least-squares fitting procedure (Figure 5a). Calculations reveal that two of the doublets (in 1:1 ratio, sub-spectra (1) and (2)) exhibit very close isomer shifts (IS, $\delta = \text{ca. } 0.4 \text{ mm/s}$) and quadrupole splittings (QS, $\Delta = \text{ca. } 0.7 \text{ mm/s}$) (Table 1). The results are consistent with the presence of high-spin iron(III) ions placed in a nearly identical octahedral environment [51] and corroborate previously reported data for ferric dimers containing two OH-bridges [52,53]. The minor sub-spectrum (3) differs from the rest, especially in the IS value. The doublet is assigned to the presence of mono-complex **1a** and its low intensity agrees well with the IR and EPR data recorded. It can be concluded that Fe(III) in **1a** is placed in a ligand environment similar to that of **1**, as no significant change in its QS value is observed.

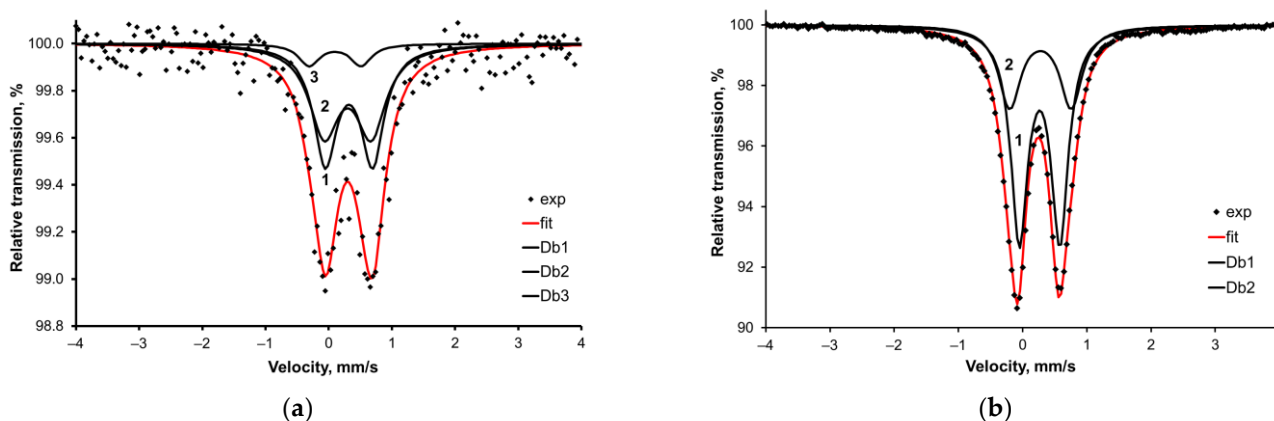


Figure 5. Mössbauer spectra at 293 K: (a) complex **1**, (b) complex **2**.

Table 1. Mössbauer parameters for solid samples **1** and **2** at 293 K (and 77 K in parentheses).

Complex	Component	δ , mm/s	Δ , mm/s	Γ , mm/s	A, %	M, %
1	Db1	0.43 (0.60)	0.75 (0.75)	0.45 (0.45)	47 (48)	0.49 (1.48)
	Db2	0.41 (0.61)	0.74 (0.79)	0.57 (0.52)	45 (47)	0.37 (1.29)
	Db3	0.21 (0.40)	0.82 (0.75)	0.40 (0.40)	8 (5)	0.09 (0.19)
2	Db1	0.37 (0.57)	0.63 (0.62)	0.32 (0.31)	66 (64)	6.96 (8.41)
	Db2	0.39 (0.58)	0.96 (1.00)	0.42 (0.38)	34 (36)	2.99 (3.91)

The Mössbauer spectrum of **2** at 293 K (Figure 5b) can be fitted in two doublets with similar IS values and 2:1 area, revealing the presence of three high-spin iron(III) ions bound in an octahedral crystal field. The QS values show that one of the metal centres is placed in a less symmetric environment than the other two. When this is compared with complex **1**, and relying on Mössbauer/EPR studies performed, it can be assumed that coordination species **2** probably belongs to the triangular iron(III) complexes of the “acetate” type, where the carboxylate groups of the antibiotic are the “main characters” in the structure formed. The formation of mixed-valence Fe(II)-Fe(III) coordination species in the case of complex **2** is ruled out due to the absence of Mössbauer signals with high IS-values ($>1.2 \text{ mm/s}$), thus directly confirming the full oxidation of Fe(II) ions under atmospheric conditions [54,55].

The increase in the isomer shift of both complexes at liquid nitrogen temperature is due to the second-order Doppler effect [56] (Figure S4). The quadrupole splitting, as expected for high-spin iron(III), does not exhibit an important temperature dependence. The average linewidth of all doublets (*ca.* 0.43 mm/s at 293 K and *ca.* 0.41 mm/s at 77 K) confirms the amorphous nature of the studied complex species.

2.2.4. Proposed Structures of Complexes 1–2

Based on the collected experimental data, we suggest that the isolated complex **1** represents a dinuclear iron(III) complex of monensin. Taking into account its composition ($\text{Fe}^{3+}:\text{Cl}^-:\text{Mon}^- = 1:1:2$) and the observed spectral results, viable architectures can be constructed as follows:

- (i) two monensinates are bound to each iron(III) ion in a bidentate manner through their terminal carboxylate and hydroxyl functions, and two chloride anions link the metal centres (Figure 6a);
- (ii) two bidentate monensinate ligands bridge the iron ions via tail hydroxyl groups and each chloride anion is terminally bound to the metal cation (Figure 6b);
- (iii) the presence of a carboxylate linker as a structural motif in **1** is excluded due to the higher Δ -value(s) detected in the IR-spectra of the solid complex.

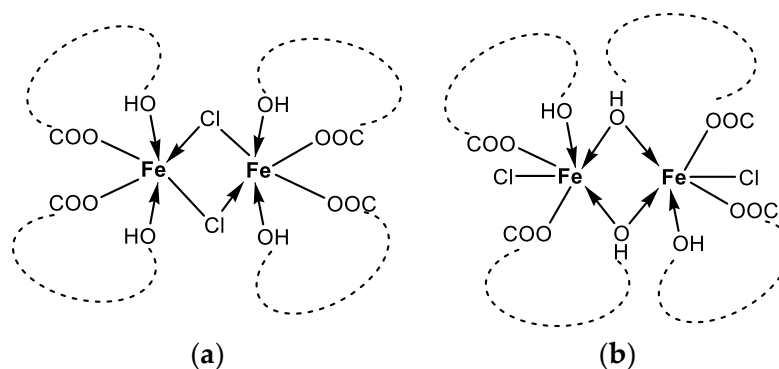


Figure 6. Proposed structure of complex **1** as dinuclear chloro-bridged (a) or hydroxyl-bridged (b) species. The monensinate skeleton is represented schematically by the dashed line connecting the terminal ligating groups.

The formation of either construct (Figure 6) can explain the observed magnetic behaviour of **1**, but to determine its most reliable structure, we applied a computational approach as described in Section 3.3.

Using the structures proposed above, we also assume that the isolation of **1** in solid state is accompanied by the presence of another type of coordination species, where the monensinate anion is bound in a similar fashion. This compound is deemed to be the mono-complex **1a** of composition $[\text{FeCl}(\text{Mon})_2]$ (Figure S2) which subsists in equilibrium with the dinuclear parent complex $[\text{FeCl}(\text{Mon})_2]_2$. Its co-precipitation cannot be controlled, but obviously its formation corroborates the observed experimental EPR and Mössbauer data, especially at low temperatures.

The spectral and microanalysis results reveal that complex **2** most likely belongs to the group of the trinuclear oxo-ferric-monocarboxylates with composition $[\text{Fe}_3(\mu_3\text{-O})(\text{Mon} \times \text{H}_2\text{O})_6(\text{H}_2\text{O})_2(\text{OH})]$ (Figure 7). We infer that each pair of ionophores serve as bridges between each pair of metal centres through the carboxylate function in a similar way to the known structure of ferric acetate. Binding of a hydroxide anion ensures the overall neutral character of the species formed. The magnetic data disclose the antiferromagnetic properties of **2**, which may arise in an indirect manner, *i.e.*, through an oxo-anion placed into the core of a trinuclear iron(III) cluster.

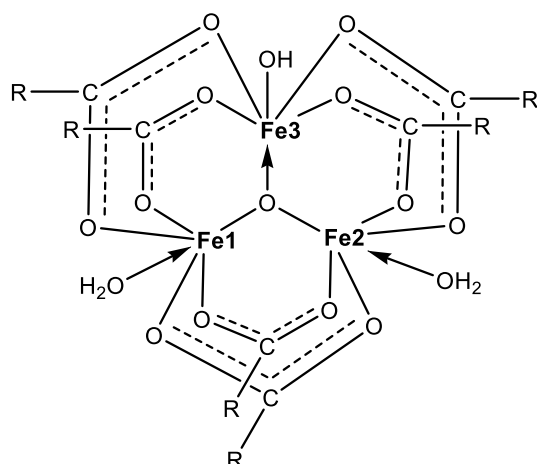


Figure 7. Proposed structure of the triangular oxo-complex **2** (R represents the polyether cavity hosting a water molecule).

To elucidate the architecture of the first coordination sphere of species **1–2**, we conducted an additional molecular modelling. As will be seen, the computed structural parameters are consistent with those observed experimentally, thus confirming the plausibility of the hypothesized constructs.

2.3. Theoretical Studies

2.3.1. Molecular Modelling of **1**

To understand the intrinsic properties of complex **1**, we built four dinuclear constructs with C_i point group symmetry as shown in Figure 8, where the monensinate binding was modelled by four acetates (representing its “head” carboxylate functions) and four ethanol molecules (as avatars of the “tail” segment hydroxyl groups). The chloride position was either bridging (**1A**) or terminal (**1B–D**). Structure **1B** comprises chloride anions which are perpendicular to the Fe_2O_6 -chromophore and occupy the axial positions in the primary coordination shell. In the other two constructs the inorganic ions lie in the plane of the diamond-core, but the carboxylate groups are parallel (**1C**) and antiparallel (**1D**) to each other.

An indication of the preferred topology of **1** can be derived from the comparison between the calculated IR spectra for **1A–D** and the experimental one. A specific feature of the experimental spectrum is the splitting of the asymmetric C=O vibration into two bands with frequencies 1594 and 1554 cm^{-1} (Figure 2), which are a good match for the corresponding computed unscaled bands for **1B–D** (Table 2). In contrast, no splitting is found in the calculated vibrational spectrum of **1A**—just a narrow band at 1613 cm^{-1} . This is a sign that the dichloro-bridged structure **1A** does not correspond to the experimentally observed vibrational behaviour of complex **1**.

Table 2. Frequencies of asymmetric stretches of the carboxylate function in monensin and similarity factors—SF (the ratio of the experimental to the calculated value for each pair of results).

Complex	Band Position, cm^{-1}		
	Exp.	Calc.	SF
1A	–	1613	–
1B (sub-band 1)	1594	1647	0.97
1B (sub-band 2)	1554	1578	0.98
1C (sub-band 1)	1594	1626	0.98
1C (sub-band 2)	1554	1604	0.97
1D (sub-band 1)	1594	1655	0.96
1D (sub-band 2)	1554	1607	0.97
2	1527	1649	0.93

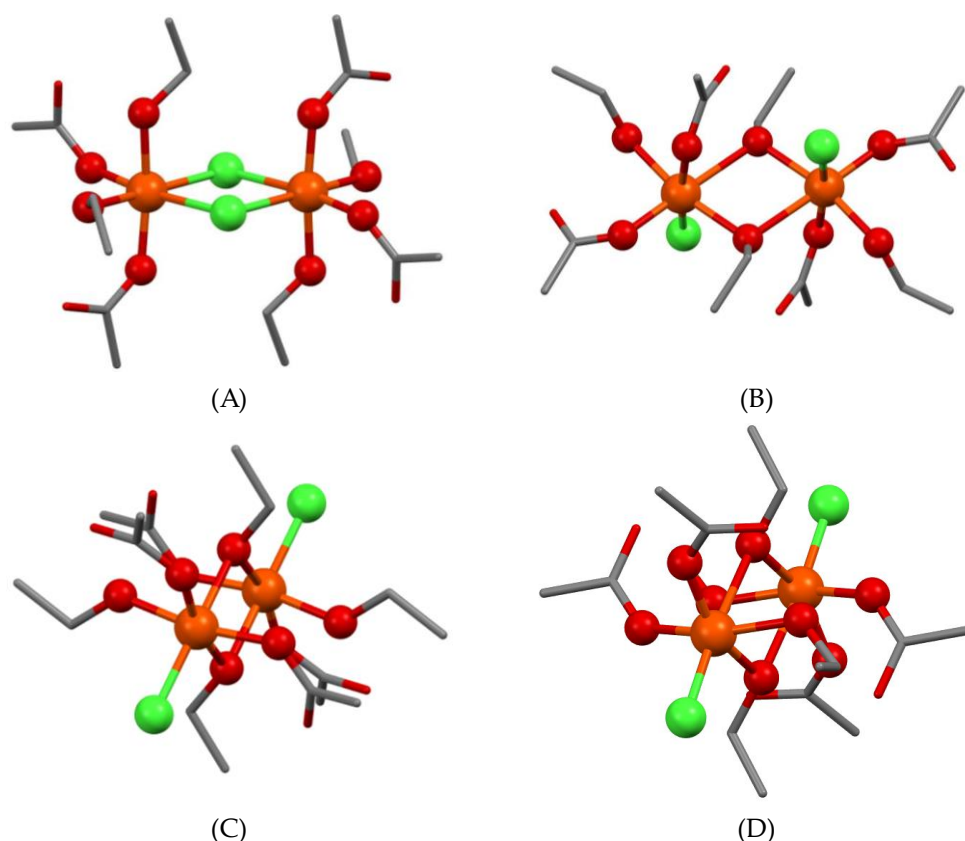


Figure 8. Modelled structures of ferric dimers **1** (A–D). Hydrogens are omitted for clarity. Colour code: C—grey, O—red, Cl—green, Fe—orange.

In order to evaluate the impact of the spin state on the EPR properties of target complex **1**, the possible states for the two high-spin Fe(III) ions ($S_{5/2}$) are taken into account, allowing for the complex to have either a ferromagnetic high spin (HS, $S_t = 10/2$) or an antiferromagnetic singlet (AFMS, $S_t = 0$) coupling (Scheme S1a). For **1A** (chloride-bridged) and **1B** (hydroxyl-bridged with axial chlorides) constructs the HS state is slightly more stable. The temperature decrease would lead to a population increase in the HS state, leading to an increased intensity of the experimental EPR signal. In the remaining models with hydroxyl oxygen linking (**1C–D**, equatorially placed chlorides), the calculated energy difference favours the low spin state at 293 K. At lower temperatures, the population of the LS state should increase and the intensity of the EPR signal should decrease with a tendency to disappear (EPR-silent state). In line with the experimental EPR data obtained (decrease in the signal at $g = 2.02$) we can conclude that complex **1** can be described as an alcohol-bridged dimer with terminally ligated chloride anions **1C–D** [57].

The comparison between the anticipated and observed properties of all modelled structures discloses that those with equatorial chlorides are the most likely. The calculated Boltzmann distribution curves show 99.80% at 293 K and 100% at 77 K in favour of **1D** over **1C**. Thus, it can be summarized that the alcohol-bridged dimer with antiparallel orientation of the carboxylates (**1D**) is the most feasible model matching the structure of complex **1**.

2.3.2. Molecular Design of **2**

As a starting construct to design the primary coordination shell of complex **2**, the crystal structure of ferric acetate [29] was used by replacing one of the water molecules with a hydroxide anion (Figure 9). The model consists of three high-spin iron ions which can interact with each other in different ways. We performed a full geometry optimization of the possible multiplicities—high spin (HS, $S_t = 15/2$) and antiferromagnetic sextet (AFMS_x, $S_t = 5/2$); the spin alignments are presented in Scheme S1b. The modelled structure belongs

to the C_{2v} symmetry point group, where two of the iron ions are equivalent with respect to the principal symmetry axis and the corresponding plane containing it. Considering the energy dependence of the spin-flip position (Table 3), the predominantly populated AFMSx is the one in which the spins flip on the iron lying on C_2 (ca. 123 kcal/mol). The state population at 293 and 77 K is calculated to be 82.9% of AFMSx (17.1% of HS) at 293 K and increases to 99.8% at 77 K.

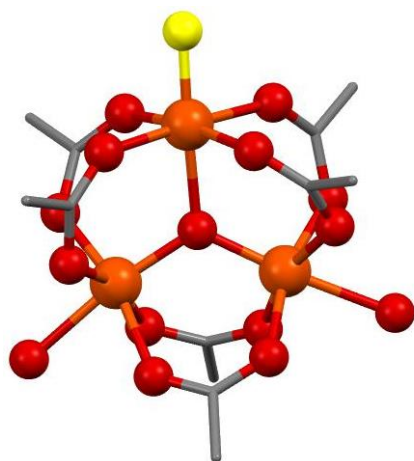


Figure 9. Modelled structure of complex 2. Hydrogens are omitted for clarity. Colour code: C—grey, O—red, Fe—orange. The hydroxide oxygen is presented in yellow.

Table 3. Enthalpy difference and calculated g-factors for the states of the proposed construct of complex 2.

Multiplicity	ΔH , kcal/mol, 293 K	g-Factor, 0 K
HS	0.91	2.005
AFMSx	0.00	2.004
AFMSx-ooa *	122.71	2.087

* Spin-flip is performed on the iron ion which does not lie on the principal axis.

To gain a deeper insight into the intimate properties of complex 2, an additional g-factor calculation was performed (Table 3), which matches well with the experimental findings (Figure 3b). The calculated value of the asymmetric C=O vibration (Table 2) is also in good agreement with the observed one.

2.4. Antibacterial Activity

The biological activity of $\text{MonH} \times \text{H}_2\text{O}$ and complexes 1–2 is evaluated in terms of their minimum inhibitory concentration (MIC), at which the tested compounds effectively inhibit the visible growth of the target Gram-positive microorganisms. In the currently applied protocol conditions, *B. cereus* (BC) appears to be more sensitive to monensic acid compared with the *B. subtilis* strain (BS) (Table 4), while the parent salts $\text{FeCl}_3 \times 6\text{H}_2\text{O}$ and $\text{FeSO}_4 \times 7\text{H}_2\text{O}$ are ineffective below 3.6–3.7 mM against both bacterial strains and the same holds for the solvent used (methanol). The studied iron(III) complexes have four- (1) and six-fold (2) increased antibacterial efficacy against *B. subtilis*, which may be due to the presence of four and six antibiotic ligands in the composition of species 1–2, respectively. On the other hand, the new coordination species are eight (1) and twelve (2) times more potent in the case of *B. cereus*—an activity that cannot be explained in terms of a simple additive effect of metal cations and ligands, linked together in the complex structures. The observed enhanced bioactivity calls for further dedicated investigation of the efficacy of the newly obtained iron(III) monensinates against different target bacterial strains/cell lines to explore their potential as suitable bioactive metal-based drugs.

Table 4. MIC of the polyether ionophore and its complexes 1–2.

Bacteria Compound	MW, g/mol	BC		BS	
		µg/mL	µM	µg/mL	µM
MonH × H ₂ O	688.90	3.91	5.67	15.63	22.69
Complex 1	2862.08	1.95	0.68	15.63	5.46
Complex 2	4363.90	1.95	0.47	15.63	3.58

3. Experimental Section

3.1. Materials and Methods

Sodium monensinate (MonNa) was generously provided by Biovet Ltd. (Huvepharma, Peshtera, Bulgaria) in a chemically pure form and was used without further purification. Monensic acid monohydrate (MonH × H₂O) was prepared by treating MonNa with HCl [58]. FeCl₃ × 6H₂O, FeSO₄ × 7H₂O, Et₄NOH, Et₃N, acetonitrile (MeCN), methanol (MeOH) p.a. grade, and CDCl₃ were delivered by local suppliers. Deionized water was used in all experiments when necessary.

The following approaches and devices were utilized in the present study: infrared spectroscopy (IR) on a Nicolet 6700 FT-IR spectrometer (Thermo Scientific, Madison, WI, USA); thermogravimetry (TG-DTA, TG-MS) on a Setaram Labsys Evo 1600 (Caluire-et-Cuire, France); electron paramagnetic resonance (EPR) on a Bruker BioSpin EMXplus10/12 EPR spectrometer (Karlsruhe, Germany); nuclear magnetic resonance (NMR) on a Bruker NEO 600 spectrometer (Karlsruhe, Germany); ⁵⁷Fe Mössbauer measurements on a Wissel spectrometer (Wissenschaftliche Elektronik GmbH, Starnberg, Germany); microanalysis on a Vario MACRO cube Elementar analysensysteme GmbH (Stuttgart, Germany) (C, H) and Perkin-Elmer SCIEX-ELAN DRC-e ICP-MS (Massachusetts, USA) (Fe). Details of the technical parameters of the spectrometers and the corresponding sample preparation procedures are described in [41,59].

3.2. Synthesis of Complexes 1–2

Complex 1: To a solution of MonH × H₂O (0.5 mmol, 344.45 mg in 15 mL MeCN), Et₄NOH (0.5 mmol, 180 µL, 40% in H₂O) was added. The reaction mixture was stirred for 15 min to ensure the deprotonation of the antibiotic and FeCl₃ × 6H₂O (0.17 mmol, 45.00 mg in 5 MeCN) was gradually added to spontaneously form an ochre solid phase. The precipitate was filtered off, washed with MeCN, and dried in a desiccator. [Fe₂Cl₂(Mon)₄]: C₁₄₄H₂₄₄Cl₂Fe₂O₄₄, MW 2862.08 g/mol. Calc. H, 8.89; C, 60.43; Cl, 2.48; Fe, 3.90%. Found: H, 8.19; C, 60.64; Cl, 2.16; Fe, 3.07%. Yield: 153.50 mg, 63%.

Complex 2: To a solution containing MonH × H₂O (0.5 mmol, 344.45 mg in 20 mL MeCN/MeOH) and Et₃N (1.0 mmol, 139.5 µL), solid FeSO₄ × 7H₂O (0.5 mmol, 139 mg) was added. The reaction mixture was stirred for 30 min until the iron salt was completely dissolved to turn the colourless solution into a yellow mixture. Subsequent addition of water afforded the formation of dark green precipitates which changed colour to tile red/rusty brown within 10–15 min, indicating Fe(II) oxidation. The solid phase was filtered off, washed with water, and dried in a desiccator. [Fe₃O(Mon × H₂O)₆(H₂O)₂(OH)]: C₂₁₆H₃₈₃Fe₃O₇₆, MW 4363.90 g/mol. Calc. H, 8.85; C, 59.45; Fe, 3.84%. Found: H, 9.68; C, 59.01; Fe, 3.94%. Yield: 327.35 mg, 90%.

3.3. Computational Protocol

The quantum chemical calculations were performed according to a previously published protocol [41]. Briefly, the geometries of all constructs were optimized with Becke's three-parameter hybrid-exchange functional combined with the Lee-Yang-Parr correlation functional [60], and with Grimme D3 correction [61] for the dispersion interactions and the 6–31G(d) basis set. Vibrational frequencies analysis was performed to verify the minima of all structures. The optimization and the vibrational spectra calculations were carried out with the software package Gaussian 16 [62]. The magnetic properties and EPR parameters for each EPR-active spin state were computed using ORCA 5.0.3 [63] with the BHandHLYP

functional [64–66] which has a higher percentage of exact Hartree–Fock exchange, the latter being of great importance for the proper estimation of the spin exchange interactions in the studied systems. The TZVP basis set of Ahlrichs and co-workers [67,68] was implemented for the ligands and the CP(PPP) basis set for the iron ions [69]. All calculations were performed in vacuo.

3.4. Antibacterial Assay

The double-layer agar hole diffusion method [70] was applied to evaluate the effect of the compounds of interest towards Gram-positive microorganisms. Two aerobic bacterial strains were used in the present study—*B. subtilis* (NBIMCC 1709) and *B. cereus* (NBIMCC 1085), supplied by the National Bank for Industrial Microorganisms and Cell Cultures (NBIMCC, Bulgaria). The antibacterial efficiency of $\text{MonH} \times \text{H}_2\text{O}$, complexes 1–2, and parent iron salts was assessed according to the protocol described in [41], replacing DMSO with MeOH as a solvent where necessary.

4. Conclusions

Two new iron(III) monensinates were synthesized and characterized via a variety of experimental methods, supplemented by molecular modelling. Common features of the obtained octahedral complexes are that (i) the monensinate ligands are bound to the iron ions via their carboxylate termini, and (ii) the ratio Fe:ligand is 1:2. However, the pattern of coordination differs. With the Fe(III) salt, an antiferromagnetic dinuclear complex is formed with metal ions also exchange-coupled by hydroxyl groups of the ligand, whereas with the Fe(II) salt a trinuclear oxo-ferric complex results, in which the iron ions, being fully oxidized by the atmospheric oxygen to Fe(III), are linked solely by the carboxylate ligand functions to form an antiferromagnetic sextet. The structure of the complexes was decoded by means of comparison between the computed characteristics of models corresponding to the elemental analysis data and the results measured with the employed experimental approaches. The antibacterial activity tests reveal that the complexes exhibit equal (against *B. subtilis*) or higher (against *B. cereus*) bioactivity, which indicates that the newly synthesized complexes may find a useful implementation as medication in the veterinary practice.

Supplementary Materials: The following supporting information can be downloaded at <https://www.mdpi.com/article/10.3390/inorganics12040114/s1>: Figure S1: Structure of monensin; Figure S2: Proposed structure of mono-complex 1a; Table S1: ^{13}C -NMR chemical shift (δ , ppm) of monensinic acid and complex 1 in CDCl_3 ($\Delta = \delta_1 - \delta_{\text{MonH}}$); Figure S3: TG-DTA/MS curves of (a) complex 1 and (b) complex 2; Figure S4: Mössbauer spectra at 77 K: (a) complex 1, (b) complex 2; Scheme S1. Electron configurations of the iron ions in (a) complex 1 and (b) complex 2.

Author Contributions: Conceptualization, N.P. and I.P.; methodology and analysis, N.P., A.T., S.S., Z.C.-Z., D.P., R.S. and R.K.; resources, P.D.; writing—original draft preparation, N.P., I.P. and A.T.; writing—review and editing, I.P. and A.T. All authors have read and agreed to the published version of the manuscript.

Funding: This research was funded by the European Union—NextGenerationEU, through the National Recovery and Resilience Plan of the Republic of Bulgaria, project SUMMIT BG-RRP-2.004-0008-C01 (№ 70-123-186).

Data Availability Statement: Data are available from the authors upon request.

Conflicts of Interest: Author Petar Dorkov is employed by the company Biovet Ltd. The remaining authors declare that the research was conducted in the absence of any commercial or financial relationships that could be construed as a potential conflict of interest. Biovet Ltd. provided the material sodium monensinate (MonNa), but the company was not involved in the study design, collection, analysis, interpretation of data, the writing of this article or the decision to submit it for publication.

References

1. Crichton, R.R.; Pierre, J.-L. Old iron, young copper: From Mars to Venus. *BioMetals* **2001**, *14*, 99–112. [[CrossRef](#)] [[PubMed](#)]
2. Crichton, R. *Iron Metabolism: From Molecular Mechanisms to Clinical Consequences*, 4th ed.; John Wiley & Sons, Ltd.: Hoboken, NJ, USA, 2016; ISBN 978-1-118-92561-4.
3. Ward, R.J.; Crichton, R.R. *Ironing Out the Brain. Metal Ions in Life Science*; De Gruyter: Berlin, Germany, 2019. [[CrossRef](#)]
4. Ward, R.J.; Dexter, D.T.; Crichton, R.R. Neurodegenerative diseases and therapeutic strategies using iron chelators. *J. Trace Elem. Med. Biol.* **2015**, *31*, 267–273. [[CrossRef](#)] [[PubMed](#)]
5. Roemhild, K.; von Maltzahn, F.; Weiskirchen, R.; Knüchel, R.; von Stillfried, S.; Lammers, T. Iron metabolism: Pathophysiology and pharmacology. *Trends Pharmacol. Sci.* **2021**, *48*, 640–656. [[CrossRef](#)]
6. Thich, J.A.; Ou, C.-C.; Powers, D.; Vasilious, B.; Mastropaolo, D.; Potenza, J.A.; Schugar, H.J. Molecular structure and magnetic properties of mu-dihydroxo-bis[2,6-pyridine dicarboxylato aquoiron(III)] and mu-dihydroxo-bis[4-hydroxo-2,6-pyridine dicarboxylato aquoiron(III)] tetrahydrate. *J. Am. Chem. Soc.* **1976**, *98*, 1425–1433. [[CrossRef](#)]
7. Ou, C.-C.; Lalancette, R.A.; Potenza, J.A.; Schugar, H.J. Molecular structure and magnetic properties of mu-dihydroxo-bis[4-dimethylamino-2,6-pyridinedicarboxylatoquo iron(III)] dihydrate, [(CH₃)₂NC₇H₂NO₄(H₂O)FeOH]₂·2H₂O. *J. Am. Chem. Soc.* **1978**, *100*, 2053–2057. [[CrossRef](#)]
8. Kato, M.; Yamada, T.; Inagaki, T.; Mori, W.; Sakai, K.; Tsubomura, T.; Sato, M.; Yano, S. Structures and magnetic properties of iron(III) dinuclear complexes with alkoxo and carboxylato bridges. *Inorg. Chem.* **1995**, *34*, 2645–2651. [[CrossRef](#)]
9. Norman, R.E.; Yan, S.; Que, L., Jr.; Backes, G.; Ling, J.; Sanders-Loehr, J.; Zhang, J.H.; O'Connor, C.J. (mu-Oxo)(mu-carboxylato) diiron(III) complexes with distinct iron sites. Consequences of the inequivalence and its relevance to dinuclear iron-oxo proteins. *J. Am. Chem. Soc.* **1990**, *112*, 1554–1562. [[CrossRef](#)]
10. Trukhan, V.M.; Gritsenko, O.N.; Nordlander, E.; Shteinman, A.A. Design and synthesis of new models for diiron biosites. *J. Inorg. Biochem.* **2000**, *79*, 41–46. [[CrossRef](#)]
11. Pardo, E.; Lloret, F.; Carrasco, R.; Muñoz, M.C.; Temporal-Sánchez, T.; Ruiz-García, R. Chemistry and reactivity of dinuclear iron oxamate complexes: Alkane oxidation with hydrogen peroxide catalysed by an oxo-bridged diiron(III) complex with amide and carboxylate ligation. *Inorg. Chim. Acta* **2004**, *357*, 2713–2720. [[CrossRef](#)]
12. Romakh, V.B.; Therrien, B.; Labat, G.; Stoekli-Evans, H.; Shul'pin, G.B.; Süß-Fink, G. Dinuclear iron, ruthenium and cobalt complexes containing 1,4-dimethyl-1,4,7-triazacyclononane ligands as well as carboxylato and oxo or hydroxo bridges. *Inorg. Chim. Acta* **2006**, *359*, 3297–3051. [[CrossRef](#)]
13. Do, L.H.; Lippard, S.J. Toward functional carboxylate-bridged diiron protein mimics: Achieving structural stability and conformational flexibility using a macrocyclic ligand framework. *J. Am. Chem. Soc.* **2011**, *133*, 10568–105681. [[CrossRef](#)] [[PubMed](#)]
14. Abe, K.; Sakiyama, S.; Nishida, T. Structural investigation of four dinuclear iron(III) complexes relevant to renal injuries. *J. Comp. Chem.* **2015**, *14*, 23–29. [[CrossRef](#)]
15. Comba, P.; Daumann, L.; Lefebvre, J.; Linti, G.; Martin, B.; Straub, J.; Zessin, T. Mono- and dinuclear copper(II) and iron(III) complexes of a tetradentate bispidine-diacetate ligand. *Aust. J. Chem.* **2009**, *62*, 1238–1245. [[CrossRef](#)]
16. Paredes-García, V.; Latorre, R.O.; Spodine, E. Electronic and magnetic properties of iron(III) dinuclear complexes with carboxylate bridges. *Polyhedron* **2014**, *23*, 1869–1876. [[CrossRef](#)]
17. Bell, M.; Edwards, A.J.; Hoskins, B.F.; Kachab, E.H.; Robson, R. Synthesis and crystal structure of a complex of a tetranucleating macrocyclic ligand which binds four NiII ions in a square arrangement with a μ₄-hydroxo group at the centre. *J. Chem. Soc. Chem. Commun.* **1987**, *24*, 1852–1854. [[CrossRef](#)]
18. Starosta, W.; Ptasiwicz-Bak, H.; Leciejewicz, J. The crystal and molecular structure of a new calcium(II) complex with pyridine-2,6-dicarboxylate, water and nitrate ligands. *J. Coord. Chem.* **2002**, *55*, 1147–1153. [[CrossRef](#)]
19. Chen, Z.-Q.; Zhang, W.-Z.; Xu, Q. Poly[[μ₂-aqua-[[μ₂-1,1'-(butane-1,4-diyl) diimidazole] bis ([μ₄-naphthalene-1,4-dicarboxylato) dimanganese(II)]. *Acta Cryst. Sect. E Struct. Rep. Online* **2008**, *64*, m1543. [[CrossRef](#)] [[PubMed](#)]
20. Shen, X.-Q.; Yao, H.-C.; Yang, R.; Li, Z.-J.; Zhang, H.-Y.; Wu, B.-L.; Hou, H.-W. Synthesis, structure and thermal properties of polynuclear complexes with a new multidentate ligand, N,N'-bis(5-ethyl-1,3,4-thiadiazol-2-yl)-2,6-pyridinedicarboxamide. *Polyhedron* **2008**, *27*, 203–209. [[CrossRef](#)]
21. Azadmehar, A.; Amini, M.M.; Hadipour, N.; Khavasi, H.R.; Fun, H.-K.; Chen, C.-J. Synthesis and structural characterization of diorganotin(IV) complexes with 2,6-pyridinedicarboxylic acid. *Appl. Organomet. Chem.* **2008**, *22*, 19–24. [[CrossRef](#)]
22. Su, Q.-J.; Li, S.-H.; Wang, L.; Xie, C.-Z.; Ouyang, Y.; Xu, J.-Y. Synthesis, structure and characterization of 1D threefold-bridging copper(II) chain with strong ferromagnetic coupling. *Inorg. Chem. Comm.* **2010**, *13*, 1210–1212. [[CrossRef](#)]
23. White, N.G.; Kitchen, J.A.; Joule, J.A.; Brooker, S. Copper-induced N–N bond cleavage results in an octanuclear expanded-core grid-like complex. *Chem. Commun.* **2012**, *48*, 6229–6231. [[CrossRef](#)] [[PubMed](#)]
24. Chen, M.; Sanudo, E.C.; Hu, J.-Y.; Hu, M.; Fang, S.-M.; Liu, C.-S. Structural diversity and magnetic properties of five Cu(II) complexes with mixed naphthalene-based dicarboxyl tecton and different N-donor co-ligands. *Aust. J. Chem.* **2013**, *66*, 963–971. [[CrossRef](#)]
25. Gou, L.; Zhang, H.-X.; Fan, X.-Y.; Li, D.-L. Lithium based coordination polymer as anode for Li-ion battery. *Inorg. Chim. Acta* **2013**, *394*, 10–14. [[CrossRef](#)]
26. Long, G.J.; Robinson, W.T.; Tappmeyer, W.P.; Bridges, D.L. The magnetic, electronic, and Mössbauer spectral properties of several trinuclear iron(III) carboxylate complexes. *J. Chem. Soc. Dalton Trans.* **1973**, *6*, 573–579. [[CrossRef](#)]

27. Boudalis, A.K.; Sanakis, Y.; Raptopoulou, C.P.; Terzis, A.; Tuchagues, J.-P.; Perlepes, S.P. A trinuclear cluster containing the $\{\text{Fe}_3(\mu_3\text{-O})\}^{7+}$ core: Structural, magnetic and spectroscopic (IR, Mössbauer, EPR) studies. *Polyhedron* **2005**, *24*, 1540–1548. [[CrossRef](#)]
28. Kantouri, M.-L.; Papadopoulos, C.D.; Hatzidimitriou, A.G.; Bakas, T.; Pachini, S. A trinuclear iron(III) complex containing the semi-cubane $[\text{Fe}_3(\mu_3\text{-O})]^{7+}$ core: Structural, spectroscopic, magnetic and electrochemical study. *Z. Für Anorg. Und Allg. Chem.* **2010**, *636*, 531–538. [[CrossRef](#)]
29. Balić, T.; Jagličić, Z.; Sadrollah, E.; Litterst, F.J.; Počkaj, M.; Baabe, B.; Kovač-Andrić, E.; Bijelić, J.; Gašo-Sokač, D.; Djerdj, I. Single crystal growth, structural characterization and magnetic properties study of an antiferromagnetic trinuclear iron(III) acetate complex with uncoordinated hexamine. *Inorg. Chim. Acta* **2021**, *520*, 120292. [[CrossRef](#)]
30. Bronstein, L.M.; Huang, X.; Retrum, J.; Schmucker, A.; Pink, M.; Stein, B.D.; Dragnea, B. Influence of iron oleate complex structure on iron oxide nanoparticle formation. *Chem. Mater.* **2007**, *19*, 3624–3632. [[CrossRef](#)]
31. Lin, M.M.; Kim, D.K. In situ thermolysis of magnetic nanoparticles using non-hydrated iron oleate complex. *J. Nanopart. Res.* **2012**, *14*, 688. [[CrossRef](#)]
32. Sánchez, M.; Sabio, L.; Gálvez, N.; Capdevila, M.; Dominguez-Vera, J.M. Iron chemistry at the service of life. *IUBMB Life* **2017**, *69*, 382–388. [[CrossRef](#)]
33. Stockwell, B.R.; Jiang, X. The chemistry and biology of ferroptosis. *Cell Chem. Biol.* **2020**, *27*, 365–375. [[CrossRef](#)] [[PubMed](#)]
34. Qiu, Y.; Cao, Y.; Cao, W.; Jia, Y.; Lu, N. The application of ferroptosis in diseases. *Pharmacol. Res.* **2020**, *159*, 104919. [[CrossRef](#)] [[PubMed](#)]
35. Guo, Q.; Li, L.; Hou, S.; Yuan, Z.; Li, C.; Zhang, W.; Zheng, L.; Li, X. The role of iron in cancer progression. *Front. Oncol.* **2021**, *11*, 778492. [[CrossRef](#)] [[PubMed](#)]
36. Wu, Z.; Zhong, M.; Liu, Y.; Xiong, Y.; Gao, Z.; Ma, J.; Zhuang, G.; Hong, X. Application of natural products for inducing ferroptosis in tumor cells. *Biotechnol. Appl. Biochem.* **2022**, *69*, 190–197. [[CrossRef](#)] [[PubMed](#)]
37. Su, Y.; Zhao, B.; Zhou, L.; Zhang, Z.; Shen, Y.; Lv, H.; Al Qudsy, L.H.H.; Shang, P. Ferroptosis, a novel pharmacological mechanism of anti-cancer drugs. *Cancer Lett.* **2020**, *483*, 127–136. [[CrossRef](#)] [[PubMed](#)]
38. Mai, T.T.; Hamai, A.; Hienzsch, A.; Cañeque, T.; Müller, S.; Wicinski, J.; Cabaud, O.; Leroy, C.; David, A.; Acevedo, V.; et al. Salinomycin kills cancer stem cells by sequestering iron in lysosomes. *Nat. Chem.* **2017**, *9*, 1025–1033. [[CrossRef](#)] [[PubMed](#)]
39. Versini, A.; Colombeau, L.; Hienzsch, A.; Gaillet, C.; Retailleau, P.; Debieu, S.; Müller, S.; Cañeque, T.; Rodriguez, R. Salinomycin derivatives kill breast cancer stem cells by lysosomal iron targeting. *Chem.-Eur. J.* **2020**, *26*, 7416–7424. [[CrossRef](#)] [[PubMed](#)]
40. Antoszczak, M.; Müller, S.; Cañeque, T.; Colombeau, L.; Dusetti, N.; Santofimia-Castaño, P.; Gaillet, G.; Puisieux, A.; Iovanna, J.L.; Rodriguez, R. Iron-sensitive prodrugs that trigger active ferroptosis in drug-tolerant pancreatic cancer cells. *J. Am. Chem. Soc.* **2022**, *144*, 11536–11545. [[CrossRef](#)] [[PubMed](#)]
41. Petkov, N.; Tadjer, A.; Encheva, E.; Cherkezova-Zheleva, Z.; Paneva, D.; Stoyanova, R.; Kukeva, R.; Dorkov, P.; Pantcheva, I. Experimental and DFT study of monensinate and salinomycin complexes containing $\{\text{Fe}_3(\mu_3\text{-O})\}^{7+}$ core. *Molecules* **2024**, *26*, 364. [[CrossRef](#)]
42. Pantcheva, I.N.; Ivanova, J.; Zhorova, R.; Mitewa, M.; Simova, S.; Mayer-Figge, H.; Sheldrick, W.S. Nickel(II) and zinc(II) dim-onensinates: Crystal structure, spectral properties and bactericidal activity. *Inorg. Chim. Acta* **2010**, *363*, 1879–1886. [[CrossRef](#)]
43. Ivanova, J.; Pantcheva, I.N.; Mitewa, M.; Simova, S.; Mayer-Figge, H.; Sheldrick, W.S. Crystal structures and spectral properties of new Cd(II) and Hg(II) complexes of monensic acid with different coordination modes of the ligand. *Centr. Eur. J. Chem.* **2010**, *8*, 852–860. [[CrossRef](#)]
44. Pantcheva, I.; Dimitrova, R.; Nedzhib, A.; Dorkov, P.; Stoyanova, R.; Zhecheva, E. Coordination compounds of polyether ionophore Monensin with gadolinium(III) ions. In *Nanoscience & Nanotechnology (Sofia)*; Balabanova, E., Mileva, E., Eds.; Acad. Evgeni Budevski Institute of Electrochemistry and Energy Systems (IEES-BAS), Bulgarian Academy of Sciences (BAS): Sofia, Bulgaria, 2019; Volume 19, pp. 40–46, ISSN 1313-8995 (print), ISSN 2738-8743 (online).
45. Pantcheva, I.; Dimitrova, R.; Ivanova, V.; Nedzhib, A.; Dorkov, P.; Dinev, D.; Spasov, R.; Alexandrova, R. Spectral properties and biological activity of La(III) and Nd(III) monensinates. *Open Chem.* **2019**, *17*, 1423–1434. [[CrossRef](#)]
46. Wojdyr, M. Fityk: A general-purpose peak fitting program. *J. Appl. Crystallogr.* **2010**, *43*, 1126–1128. [[CrossRef](#)]
47. Muralidhara, R.S.; Kesavulu, C.R.; Rao, J.L.; Anavekar, R.V.; Chakradhar, R.P.S. EPR and optical absorption studies of Fe^{3+} ions in sodium borophosphate glasses. *J. Phys. Chem. Solids* **2010**, *71*, 1651–1655. [[CrossRef](#)]
48. Kakazey, M.; Vlasova, M.; Gonzalez-Rodriguez, G.; Salazar-Hernández, B. Fine structure of EPR spectra of Fe^{3+} in $\alpha\text{-Al}_2\text{O}_3$ crystal, powders, and textured ceramics. *Mat. Sci. Engin.* **2002**, *90*, 114–119. [[CrossRef](#)]
49. Borer, L.; Thalken, L.; Zhang, J.H.; Reiff, W.M. Characterization of a dimeric iron(III) complex of N,N'-ethylenebis(salicylamine). *Inorg. Chem.* **1983**, *22*, 3174–3176. [[CrossRef](#)]
50. Vercaemer, V.; Lelong, G.; Hijjiya, H.; Kondo, Y.; Galois, L.; Calas, G. Diluted Fe^{3+} in silicate glasses: Structural effects of Fe-redox state and matrix composition. An optical absorption and X-band/Q-band EPR study. *J. Non-Cryst. Solids* **2015**, *428*, 138–145. [[CrossRef](#)]
51. Murray, K.S. Binuclear oxo-bridged iron(III) complexes. *Coord. Chem. Rev.* **1974**, *12*, 1–35. [[CrossRef](#)]
52. Rodriguez, F.; Moreno, M. The influence of water addition on solutions of FeCl_3 in isopropanol. *Z. Für Naturforschung* **1983**, *38*, 701–702. [[CrossRef](#)]
53. Vertes, A.; Korecz, L.; Burger, K. *Mössbauer Spectroscopy*; Elsevier: Amsterdam, The Netherlands, 1979.

54. Reedijk, J.; van Der Kraan, A.M. Mössbauer effect of octahedral iron(II) solvates. *Recl. Trav. Chim. Pays-Bas.* **1969**, *88*, 828–832. [[CrossRef](#)]
55. Goldanskii, V.I.; Herber, R.H. *Chemical Applications of Mossbauer Spectroscopy*; Academic Press: Cambridge, MA, USA, 1968.
56. Greenwood, N.N.; Gibb, T.C. *Mössbauer Spectroscopy*; Chapman and Hall: London, UK, 1971.
57. You, Z.-L.; Zhu, H.-L. A dinuclear Schiff base iron(III) complex with the ligand N,N'-bis(2-oxidophenylmethyleneimino) propane-1,2-diamine. *Acta Cryst. Sect. E: Struct. Rep. Online* **2004**, *60*, m1046–m1048. [[CrossRef](#)]
58. Gertenbach, P.G.; Popov, A.I. Solution chemistry of monensin and its alkali metal ion complexes. Potentiometric and spectroscopic studies. *J. Am. Chem. Soc.* **1975**, *97*, 4738–4744. [[CrossRef](#)]
59. Petkov, N.; Pantcheva, I.; Ivanova, A.; Stoyanova, R.; Kukeva, R.; Alexandrova, R.; Abudalleh, A.; Dorkov, P. Novel cerium(IV) coordination compounds of monensin and salinomycin. *Molecules* **2023**, *28*, 4676. [[CrossRef](#)] [[PubMed](#)]
60. Stephens, P.J.; Devlin, F.J.; Chabalowski, C.F.; Frisch, M.J. Ab initio calculation of vibrational absorption and circular dichroism spectra using density functional force fields. *J. Phys. Chem.* **1994**, *98*, 11623–11627. [[CrossRef](#)]
61. Grimme, S.; Antony, J.; Ehrlich, S.; Krieg, H. A consistent and accurate ab initio parametrization of density functional dispersion correction (DFT-D) for the 94 elements H-Pu. *J. Chem. Phys.* **2010**, *132*, 154104. [[CrossRef](#)] [[PubMed](#)]
62. Frisch, M.J.; Trucks, G.W.; Schlegel, H.B.; Scuseria, G.E.; Robb, M.A.; Cheeseman, J.R.; Scalmani, G.; Barone, V.; Petersson, G.A.; Nakatsuji, H.; et al. *Gaussian 16, Revision B.01*; GaussView 5.0.; Gaussian, Inc.: Wallingford, CT, USA, 2016.
63. Neese, F. Software update: The ORCA program system—Version 5.0. *WIREs Comp. Mol. Sci.* **2022**, *12*, e1606. [[CrossRef](#)]
64. Becke, A.D. A new mixing of Hartree-Fock and local density-functional theories. *J. Chem. Phys.* **1993**, *98*, 1372–1377. [[CrossRef](#)]
65. Yang, Y.; Ratner, M.A.; Schatz, G.C. Computational modeling of octahedral iron oxide clusters: Hexaaquairon(III) and its dimers. *J. Phys. Chem. C* **2013**, *117*, 21706–21717. [[CrossRef](#)]
66. Zhao, H.; Fang, C.; Gao, J.; Liu, C. Spin-state energies of heme-related models from spin-flip TDDFT calculations. *Phys. Chem. Chem. Phys.* **2016**, *18*, 29486–29494. [[CrossRef](#)]
67. Schaefer, A.; Horn, H.; Ahlrichs, R. Fully optimized contracted Gaussian-basis sets for atoms Li to Kr. *J. Chem. Phys.* **1992**, *97*, 2571–2577. [[CrossRef](#)]
68. Schaefer, A.; Huber, C.; Ahlrichs, R. Fully optimized contracted Gaussian-basis sets of triple zeta valence quality for atoms Li to Kr. *J. Chem. Phys.* **1994**, *100*, 5829–5835. [[CrossRef](#)]
69. Neese, F. Prediction and interpretation of the ⁵⁷Fe isomer shift in Mössbauer spectra by density functional theory. *Inorg. Chim. Acta* **2002**, *337*, 181–192. [[CrossRef](#)]
70. Andrews, J.M. Determination of minimum inhibitory concentrations. *J. Antimicrob. Chemother.* **2001**, *48* (Suppl. S1), 5–16. [[CrossRef](#)] [[PubMed](#)]

Disclaimer/Publisher's Note: The statements, opinions and data contained in all publications are solely those of the individual author(s) and contributor(s) and not of MDPI and/or the editor(s). MDPI and/or the editor(s) disclaim responsibility for any injury to people or property resulting from any ideas, methods, instructions or products referred to in the content.